The role of brines in gas adsorption and dissolution in kerogen nanopores for enhanced gas recovery and CO_2 sequestration

Juan Zhou[a], Zhehui Jin[b,*], Kai H. Luo[c,*]

[a] Center for Combustion Energy, Key Laboratory for Thermal Science and Power Engineering of Ministry of Education, Department of Energy and Power Engineering, Tsinghua University, Beijing 100084, China

[b] School of Mining and Petroleum Engineering, Department of Civil and Environmental Engineering, University of Alberta, Edmonton, Alberta T6G 1H9, Canada

[c] Department of Mechanical Engineering, University College London, Torrington Place, London WC1E 7JE, UK

*Corresponding author: Kai H. Luo

Address: Department of Mechanical Engineering, University College London, Torrington Place, London

Fax number: +44 (0)20 7388 0180

Email: K.Luo@ucl.ac.uk

*Corresponding author: Zhehui Jin

Address: School of Mining and Petroleum Engineering, Department of Civil and Environmental Engineering, University of Alberta, Edmonton

Fax number: +1 780-492-6633

Email: zhehui2@ualberta.ca

Abstract

Understanding storage characteristics of CH_4 and CO_2 in shale media is important for enhanced gas recovery and geological CO_2 sequestration. This work reports a molecular simulation study of CH_4 and CO_2 storage behaviors in kerogen nanopores partially saturated with brines. Molecular distributions of pure CH_4, pure CO_2 and their mixtures in the kerogen nanopores are quantified and divided into three distinct zones: adsorption between kerogen surfaces in Zone 1, aggregation at the kerogen-brine (water) interface in Zone 2, and gas dissolved in the confined brine in Zone 3. The gas uptake is found to be affected by two different types of storage mechanisms: adsorption (i.e. in Zone 1) and dissolution (i.e. in Zones 2 and 3). Uptake of CH_4 and CO_2 decreases linearly with increasing salinity, but with different mechanisms. CH_4 uptake is dominated by its adsorption in Zone 1, where its density distribution is not affected, but the available volume decreases as salinity increases. On the other hand, CO_2 solubility in brine contributed by Zone 2 and Zone 3 can be comparable to its adsorption in Zone 1. As salinity increases, significant decrease in CO_2 solubility in brine is observed, besides the available volume reduction in Zone 1. For mixture sorption, the CO_2 density is enhanced in the region of CH_4/CO_2/brine (water) interface, while that of CH_4 slightly decreased. Furthermore, increasing salinity leads to decreased amounts of recovered CH_4 and sequestrated CO_2. Our work provides new and important insights into enhanced gas recovery by CO_2 injection and geological CO_2 sequestration in shale reservoirs.

Keywords: Molecular simulation; Enhanced gas recovery; CO_2 sequestration; Adsorption; Dissolution; Salinity

1. Introduction

Driven by the sustained economic development, the global energy consumption has been growing continuously [1]. As a result, CO_2 emissions from fossil fuel combustion have created many environmental concerns. CO_2 enhanced shale gas recovery (CO_2-ESGR) is regarded as a promising technology which can not only satisfy the ever-growing global energy demands, but also mitigate the global warming and climate change by injecting CO_2 into the underground [2,3]. The injected CO_2 is capable of promoting shale gas production [4]. In the meantime, depleted shale gas reservoirs possess huge potentials for geological CO_2 sequestration [5]. Besides, the enhanced CH_4 production can help offset the cost of CO_2 sequestration, which makes it economically more viable [6].

Shale gas is mainly composed of CH_4. Kerogen makes up the majority of organic matters in shale and has been reported to have a significant number of nanopores, which is recognized as the main storage site for shale gas [7,8]. Shale gas storage has been classified into three distinct forms: gas adsorption on pore surfaces, free gas filling in open pores and microcracks, and dissolved gas in formation fluid and kerogen matrix [9]. Generally, adsorption is thought to play a crucial role in the total gas uptake due to the strong fluid-surface interactions in nanopores [10,11] and the larger adsorption capacity of CO_2 than CH_4 makes it possible for CO_2-ESGR [12–14]. On the other hand, kerogen can be partially saturated with formation water (brine) due to the presence of connate water and hydraulic fracturing, which carries varying degrees of salinity [21–23], while CO_2 solubility trapping is one of the key geological CO_2 sequestration mechanisms [19]. Therefore, understanding the mechanisms for gas storage in kerogen nanopores is essential to determining shale gas production and the potential of geological CO_2 sequestration in depleted shale gas reservoirs.

Many experimental studies have been conducted on the adsorption of CH_4 and CO_2 in shale at a macroscale level, such as measuring gas uptake in shale samples under controlled temperature and

pressure conditions. Previous research showed that the total organic carbon (TOC) is a key factor controlling the gas uptake in shale and a strong positive correlation of sorption capacities for both CH_4 and CO_2 with TOC has been widely reported [18,20–22]. Many experiments have addressed the moisture effect on gas adsorption by comparing the adsorption capacities in dry and moisture equilibrated shale samples [18,20,23–26]. The results generally indicated that the presence of water results in lower gas adsorption capacities by occupying the pore volume and competing for adsorption sites. These experimental studies have shed light on the macroscopic adsorption properties of CH_4 or CO_2 in kerogen or shale samples. However, experimental techniques have some inherent limitations in probing the microscopic mechanisms of gas adsorption and recovery process.

Molecular simulation approaches, such as molecular dynamics (MD) and grand canonical Monte Carlo (GCMC) simulations, can provide useful information from a molecular perspective. To represent kerogen nanopores, simplified carbon slit models have been widely used in previous studies. Kurniawan *et al*. [27] studied the adsorption of CH_4 and CO_2 in carbon slit pores and found that the interaction potential between CO_2 and the pore surface is much stronger than that between CH_4 and pore surface. Similar trends were also reported in other simulation works [28]. A realistic kerogen matrix is far more complicated than the perfect graphite surface in terms of chemical compositions and structural properties. Zhao *et al*. [29] investigated the effect of moisture content on the adsorption behavior of CH_4 in type II kerogen matrix. They reported that the CH_4 adsorption capacity on moist kerogen decreases with the increasing moist content. Similar conclusions were also obtained for CH_4 and CO_2 adsorption in Huang *et al*. [30]. Zhou *et al*. [31] also studied the moisture effect on the CH_4/CO_2 adsorption in kerogen slit pores. Water forms clusters in the middle of kerogen slit pores, which reduces CH_4 pore filling, thereby leading to a decrease in the CH_4 adsorption capacity. For CH_4/CO_2 binary mixtures, CH_4 adsorption capacity decreases as the moisture content increases,

whereas the effect of moisture on CO_2 adsorption capacity depends on its mole fractions. In general, previous studies on gas adsorption reported a negative effect of moisture on CH_4 and CO_2 adsorption capacity, while they generally ignored gas dissolution in water. On the other hand, a number of studies reported an enhanced CH_4 and CO_2 solubility in nanopores filled with water. For example, Liu et al. [32] reported that CH_4 solubility in water confined in nano-porous silica materials can be two to three orders of magnitude higher than its bulk solubility. Besides, enhanced CH_4 and CO_2 solubility in water confined in zeolites and metal−organic frameworks [33] as well as clay interlayer nanopores [34] have been reported. In other words, the brine confined in kerogen nanopores may dissolve a non-negligible amount of CO_2. Moreover, in these studies, pure water has been commonly used, which cannot represent the formation water in shale reservoirs which is highly saline [35–37], with its salinity increasing with the burial depth [35,38]. When CO_2 is injected, it gets in contact with brine. Both moisture and salinity could affect the adsorption and dissolution of CH_4 and CO_2 in kerogen nanopores and subsequently affect CH_4 recovery and geological CO_2 sequestration. Thus, it is imperative to explicitly study the effect of brine salinity on gas adsorption and dissolution in an integrated manner to reveal the underlying mechanisms of enhanced gas recovery by CO_2 injection and geological CO_2 sequestration in partially saturated kerogen nanopores.

Therefore, the current study aims to investigate the effect of salinity on adsorption and dissolution of pure and binary mixtures of CH_4 and CO_2 in kerogen nanopores in the presence of brine by using GCMC simulations under typical shale reservoir conditions (338.15 K and pressure up to 60 MPa). This work attempts to provide potential guidance for CH_4 recovery and geological CO_2 sequestration in shale reservoirs. Previous studies suggested that slit-shaped pores constitute the majority of the pore structures in shale formations [39–41]. Thus, in this work, an atomic model of kerogen slit nanopores is created to describe the common pore structures in organic matters. NaCl solutions of varying salinity

are used to represent brine. The adsorption behaviors of pure CH_4, pure CO_2 and their binary mixtures in the kerogen slit pores filled with brines of varying ion concentrations are analyzed systematically. We use 2 nm kerogen slit nanopores to study the storage mechanisms of CH_4 and CO_2 in the presence of brine. The pore system in shale is commonly characterized by micropores (pore diameter <2 nm), mesopores (2–50 nm), and macropores (larger than 50 nm) [13]. The 2 nm kerogen pores are used as a representative of micropores, which have relatively large pore volume and specific surface area, regarded as the main gas storage space [42]. Interactions between CH_4, CO_2, brine, and kerogen are discussed in details. Moreover, the salinity effect on CH_4 recovery and CO_2 sequestration is assessed.

2. Methodology

2.1. Construction of kerogen slit nanopores

The over-mature type II kerogen in the gas window with high potential in producing shale gas, is selected in this work. The corresponding molecular model proposed by Ungerer *et al*. [43] based on experimental data [44] is adopted to build kerogen matrixes and slit nanopores. The kerogen chemical formula is $C_{175}H_{102}O_9N_4S_2$ and its molecular structure is shown in **Fig. 1a**.

The kerogen matrix is generated by performing MD simulations in the canonical ensemble (NVT) and the isobaric isothermal ensemble (NPT) using the LAMMPS package [45]. The time step for all MD simulations is 1 fs. The Dreiding force field [46] is adopted to calculate kerogen intramolecular interactions. Firstly, the initial structure of kerogen macromolecule is relaxed individually by NVT-MD simulations. Then, 160 relaxed kerogen molecules are randomly placed in a large simulation box of $20 \times 20 \times 20$ nm^3 and NVT simulations are conducted at 900 K for 250 ps. The final configuration of the kerogen matrix is generated following the MD relaxation procedure proposed by Collell *et al*. [47]. The density of the final kerogen matrix converges to 1.24 g/cm^3, which is within the range of mature kerogens (1.18 ~1.35 g/cm^3) [48]. The kerogen matrix is extended in the *Z*-direction to create

a slit pore as illustrated in **Fig. 1b**. Slit models with a pore width of 2 nm are selected. The pore width W is defined as the distance between the very last atoms from each kerogen surface in the *Z*-direction. The kerogen slit pore is then filled with brines of different salinities (0 M for pure water, 2.03 M, 4.06 M and 6.09 M), assuming that the amount of pre-adsorbed water/brine remains constant during simulations. NaCl aqueous solution is selected to represent the brine in kerogen [38]. In detail, 1970 water molecules as well as 0, 72, 144 and 216 pairs of Na^+ and Cl^- ions are placed in the space between two kerogen sheets, corresponding to the salinity of 0 M, 2.03 M, 4.06 M and 6.09 M, respectively. The brine densities within nanopores are 0.451 g/cm^3 for pure water, 0.505, 0.558 and 0.612 g/cm^3 for 2.03 M, 4.06 M and 6.09 M, respectively, which are defined as the total mass of brine per unit pore volume.

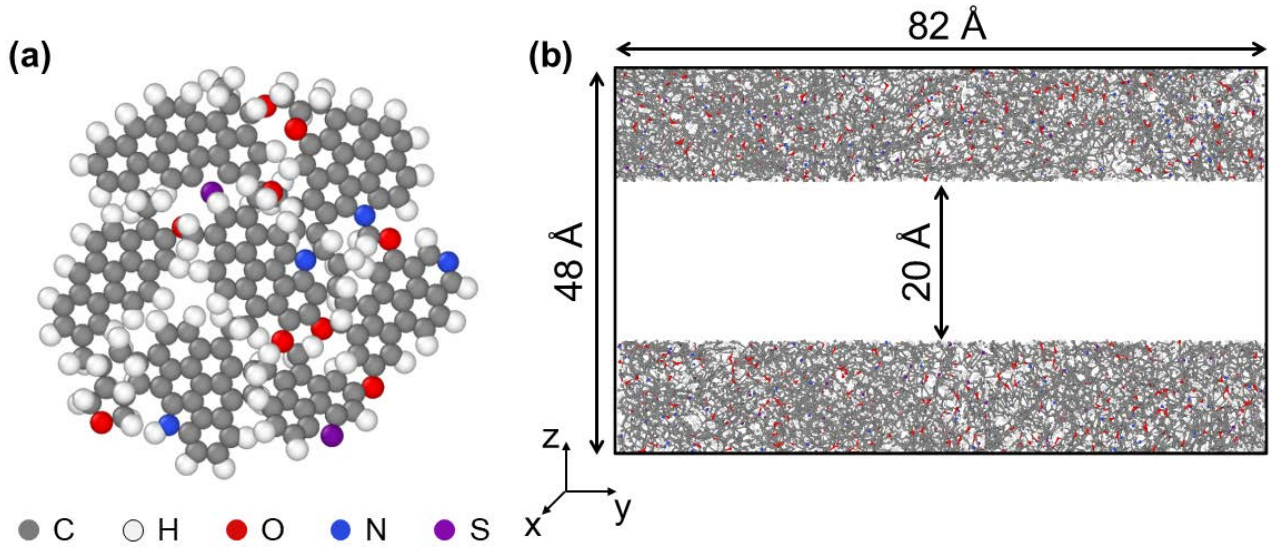

Fig. 1. (a) Molecular model of type II-D kerogen. (b) Molecular model of the kerogen slit nanopore. The pore width is 2 nm. Carbon atoms are represented by gray, hydrogen by white, oxygen by red, nitrogen by blue, and sulfur by purple spheres, respectively.

2.2. Intermolecular Interactions

The TraPPE-UA force field [49] is adopted for CH_4 molecules. The CO_2 molecules are described by a rigid TraPPE model [50]. The length of the C-O bond and the O-C-O bending angle are fixed as 1.16 Å and 180°, respectively. For water molecules, the simple point charge extended model (SPC/E)

[51] is chosen, in which the O-H bond length is 1 Å and the H-O-H bending angle is 109.47º. The Smith-Dang potentials [52] are applied for Na^+ and Cl^- ions. The Lennard-Jones (LJ) parameters are summarized in **Table 1**. The Lorentz-Berthelot mixing rules [53] are employed to calculate the interactions between unlike atoms. The non-bonded interactions include contributions from the short-range interactions (LJ 12-6 potential energy) and the Coulombic (electrostatic) interactions. A cutoff radius of 1.4 nm is used to compute LJ interactions with a tail correction [54]. The Coulombic energy is computed using the Ewald summation method [55].

Table 1 The LJ parameters and partial charges [49–52]

Atom	ε/k_B (K)	σ (Å)	q (e)
CH_4	148.0	3.73	0.00
C-CO_2	27.0	2.80	+0.70
O-CO_2	79.0	3.05	-0.35
O-H_2O	78.18	3.166	-0.8476
H-H_2O	0	0	+0.4238
Na^+	65.42	2.35	+1.0
Cl^-	50.32	4.4	-1.0

2.3. Simulation details

The systems containing brines of varying salinities are first equilibrated through a 26-ns NVT MD simulation at 338.15 K. The kerogen sheets are rigid, while water molecules and ions are allowed to move freely. Subsequently, the produced configurations are used for gas adsorption in kerogen slit pores. GCMC simulations are carried out to simulate the adsorption of pure CH_4, pure CO_2 and CH_4/CO_2 mixtures in kerogen slit pores filled with brines at 338.15 K. The GCMC technique is a stochastic method that simulates a system with a constant volume V in equilibrium with an infinite

reservoir imposing chemical potential μ and system temperature T [56]. During GCMC simulations, kerogen is treated as a rigid material. For each system, the numbers of water molecules and ions are constant, assuming that the brine remains within the pore during the gas recovery and CO_2 sequestration process. For CH_4, three types of moves are attempted, including translation, insertion, and deletion, whereas for CO_2 and H_2O molecules, rotational moves are additionally implemented. For Na^+ and Cl^- ions, only translational moves are applied. A total number of 40,000 cycles per fluid molecule is carried out for each pressure condition, with the first half used for the equilibration stage and the second half for the sampling stage. The gas chemical potentials are obtained by the Widom's insertion method [57,58] using Monte Carlo simulations in the NVT ensemble, where the fluids are simulated in the bulk phase. The density of bulk mixtures is calculated by the Peng−Robinson equation of state (PR-EOS) [59]. MCCCS Towhee [60] is applied in all the MC simulations.

Helium adsorption [61,62] is used to estimate the effective pore volume within kerogen slit pores with water/brine filled. Helium is assumed to be a non-adsorbing gas and its solubility in water is negligible [63,64]. The pore volume can be calculated based on the number of helium molecules filled within the kerogen pores (excluding those in the kerogen matrix),

$$V_p = \frac{\langle N_{\mathrm{He}} \rangle}{\rho_{\mathrm{He,bulk}}}, \tag{1}$$

where $\langle N_{\mathrm{He}} \rangle$ is the ensemble-averaged number of helium molecules filled in kerogen nanopores, and $\rho_{\mathrm{He,bulk}}$ is the bulk number density of helium at given temperatures and pressures. Detailed simulation parameters of helium adsorption in kerogen can be found in our previous work [65]. Effective pore volumes of the moist kerogen slit pores as a function of salinity are plotted in **Fig. S1**. The effective pore volume decreases linearly with salinity.

3. Results and Discussion

In this section, we first investigate the single-component gas uptake of CH_4 and CO_2, and then CH_4/CO_2 binary mixtures in kerogen nanopores. The effect of salinity is analyzed in detail. In the last part, the salinity effects on CH_4 recovery and CO_2 sequestration during pressure drawdown and CO_2 injection processes are discussed.

3.1. Adsorption and dissolution of pure gases in kerogen nanopores

The equilibrium configurations of CH_4 and brine in kerogen nanopores at 338.15 K and 40 MPa are shown in **Fig. 2**. Due to high water/brine content, large water/brine clusters form in the middle of the pore and ions are distributed evenly within. Compared to our previous work [31] with a lower water density, water/brine clusters in this work are much wider and large areas of water/brine clusters are in contact with the kerogen surface. CH_4 molecules surround each water/brine cluster but negligible intermolecular diffusion has occurred. Equilibrium snapshots of CO_2 and brine in kerogen nanopores at 338.15 K and 40 MPa are shown in **Fig. 3**. Similarly, a large water/brine cluster is formed in the middle of each pore and occupies a large volume. There is a significant difference, however, between **Figs. 2** and **3**, that CO_2 molecules in the CO_2/brine(water)/kerogen system wrap tightly around the water/brine cluster, especially under low salinities. This is because CO_2 has a stronger affinity than CH_4 to both water/brine and kerogen surface.

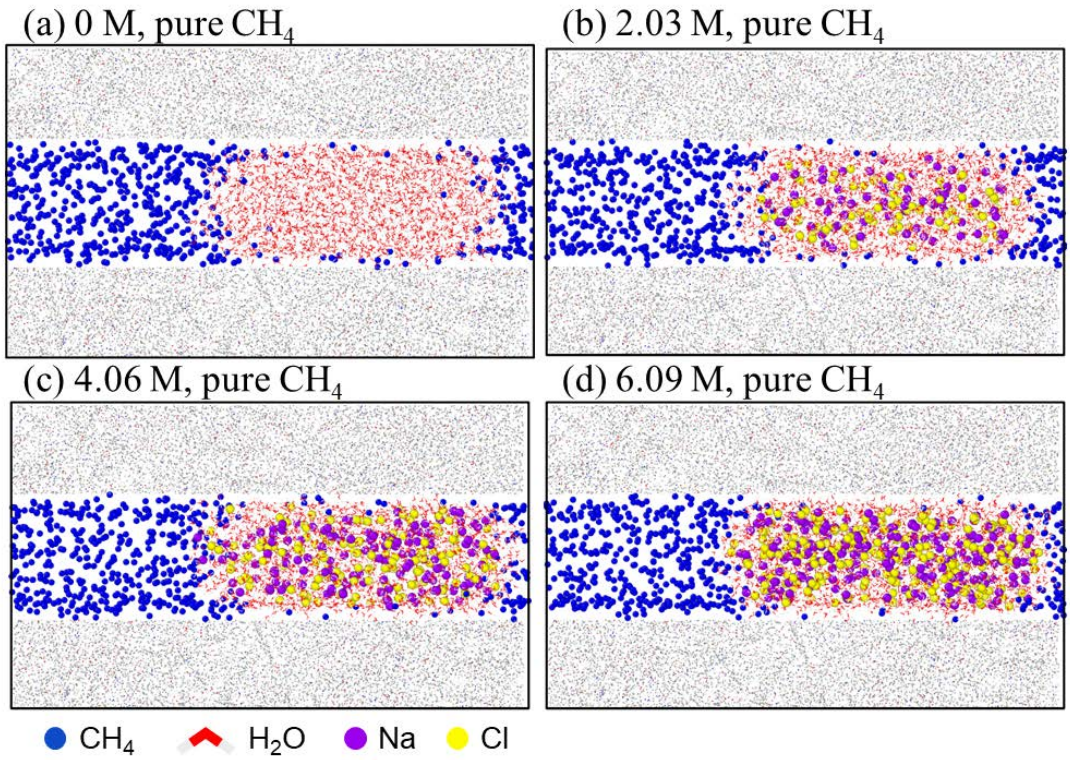

Fig. 2. Equilibrated snapshots of CH_4 and brine in kerogen nanopores with different salinities: (a) 0 M; (b) 2.03 M; (c) 4.06 M; (d) 6.09 M at 338.15 K and 40 MPa with an average H_2O density of 0.451 g/cm^3 within kerogen nanopores.

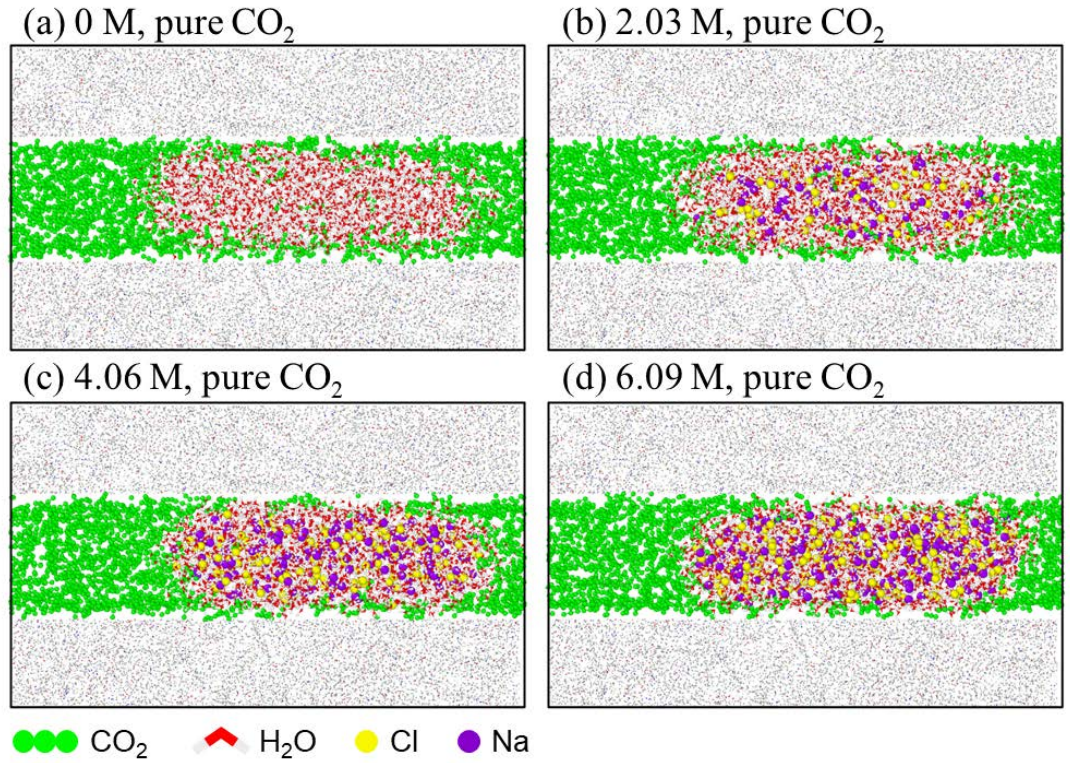

Fig. 3. Equilibrated snapshots of CO_2 and brine in kerogen nanopores with different salinities: (a) 0 M; (b) 2.03 M; (c) 4.06 M; (d) 6.09 M at 338.15 K and 40 MPa with an average H_2O density of 0.451 g/cm^3 within kerogen nanopores.

The total gas uptake of pure CH_4 and CO_2 in moist kerogen nanopores with varying brine salinities under different pressures is plotted in **Fig. 4**. Under the same pressure and salinity, pure CO_2 uptake is much larger than that of CH_4. Both CH_4 and CO_2 uptakes decrease linearly with salinity. In **Fig. 5**, we present the 2-D density contour plots of pure CH_4 and CO_2 at 338.15 K and 40 MPa. For clarity, the kerogen sheets are not shown. We find that the CH_4 density is close to 0 at the center of the pore, where the water/brine clusters reside. In **Fig. 5a**, an extremely thin CH_4 layer forms between the water/brine cluster and kerogen surfaces. As salinity increases, the CH_4 layer becomes thinner and nearly disappears at 6.09 M as shown in **Fig. 5d**. On both sides of the water/brine cluster, the CH_4 density near the kerogen surface is very high with an obvious adsorption layer, which is similar to the dry conditions as reported in Jiang *et al*. [66]. For CO_2, as depicted in **Figs. 5e-f**, a very distinct CO_2 layer is formed at the kerogen-brine (water) interface as in Li *et al*. [67]. Similar to CH_4, this layer becomes thinner as salinity increases. On both sides of the water/brine cluster, CO_2 density is higher than that of CH_4 and the adsorption layers are more obvious.

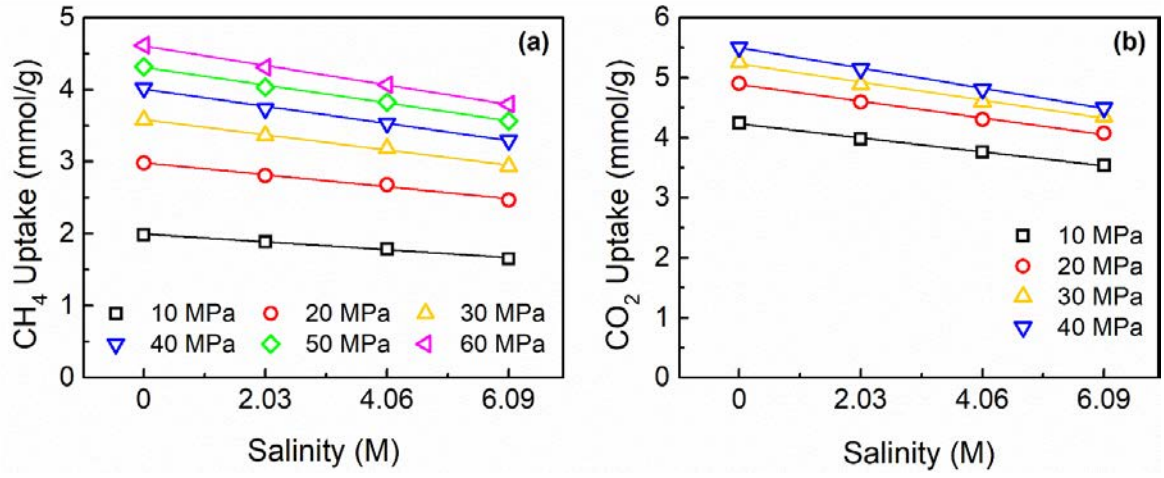

Fig. 4. Uptake of (a) CH_4; (b) CO_2 in kerogen nanopores under various pressures and salinities at 338.15 K. The scatter points are obtained from GCMC simulations and the lines are from linear fitting.

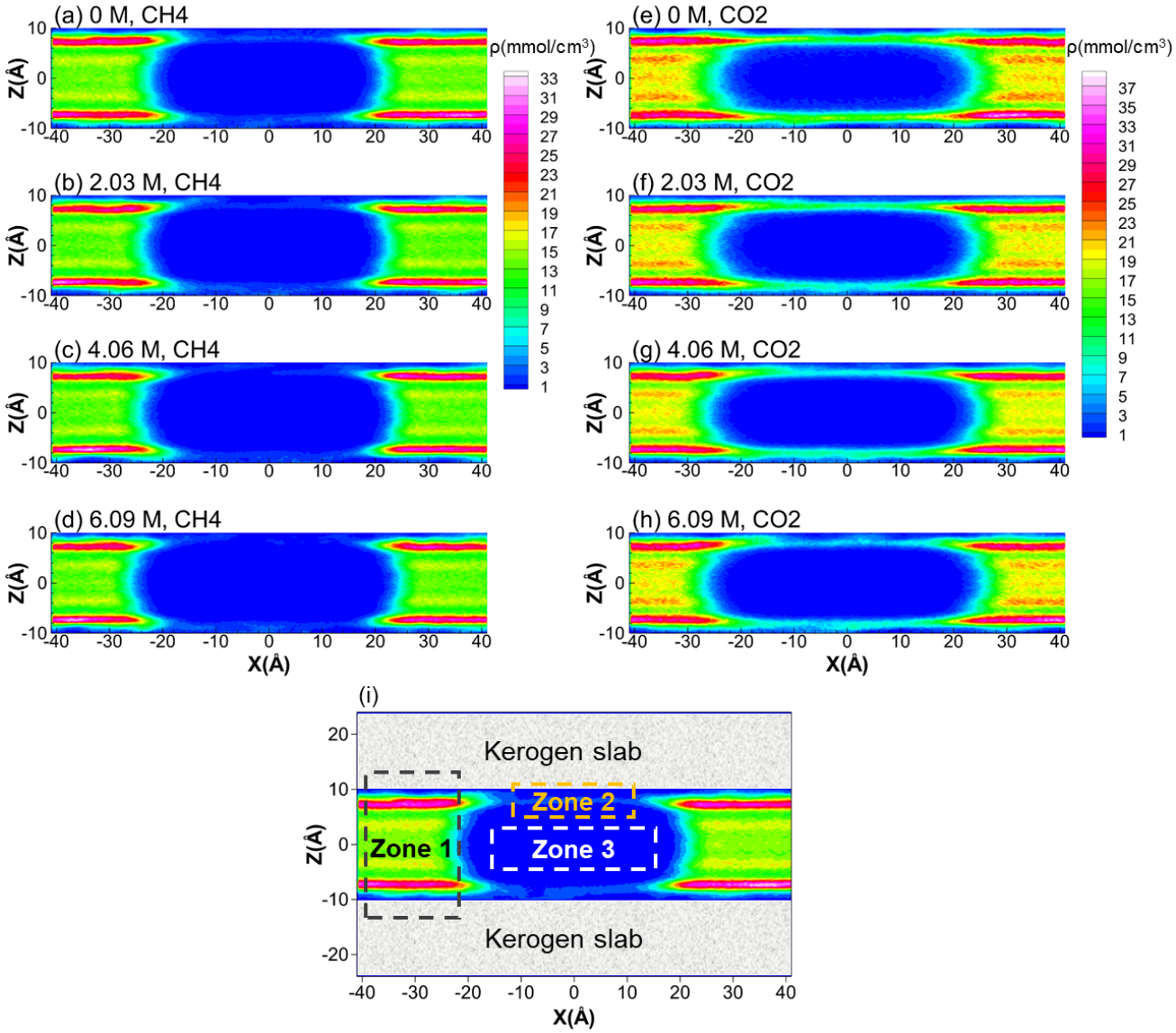

Fig. 5. Two-dimensional contour plots of CH_4 (a-d) and CO_2 (e-h) density distributions in 2-nm kerogen pores under different salinities at 338.15 K and 40 MPa. (i) Schematic diagram of three distinctive zones of CH_4 and CO_2 distributions in a 2 nm moist kerogen pore. The position X = 0 Å, Z = 0 Å dictates the center of the pore.

According to the distributions of CH_4 and CO_2 in kerogen slit pores, their density profiles can be divided into three distinct zones as presented in **Fig. 5i**. Zone 1 consists of the gas molecules adsorbed in the pore space away from the water/brine cluster. Zone 2 represents the gas molecules accumulating at kerogen-brine (water) interfaces. Zone 3 contains the gas molecules dissolved in the water/brine cluster. As in the previous study [67], gas molecules in Zone 2 and Zone 3 can be denoted as dissolved gas in confined brine. To better study the salinity effect, density profiles of CH_4 and CO_2 in these three

zones along the *Z*-direction are plotted in **Figs. 6** and **7**, respectively. The density profiles in Zone 1 are given as those at X = -34 Å, while those in Zones 2 and 3 are at X = 0 Å. As shown in **Fig. 6a**, there is only a slight decrease in the CH_4 density in Zone 1 with the addition of NaCl. As salinity further increases, such a trend is not obvious. In Zone 2, the CH_4 density corresponds to the thin CH_4 layer in **Fig. 5**. As salinity increases, the CH_4 density in Zone 2 slightly decreases. Combining **Fig. 6b** and **Fig. 6c**, we find that in Zone 2, CH_4 and H_2O co-adsorb on the kerogen surfaces. In Zone 3 (see **Fig. 6b**), the CH_4 density is close to 0, indicating that only a small number of CH_4 molecules are dissolved in the water/brine cluster.

For CO_2, **Fig. 7a** dictates that the trend of CO_2 density in Zone 1 is similar to that of CH_4 except that the decrease in CO_2 density is more obvious upon the addition of ions. As can be seen in **Fig. 7b**, the density of the CO_2 layer in Zone 2 is comparable to that in Zone 1. As salinity increases, CO_2 density in Zone 2 decreases. Interestingly, in contrast to the CH_4 case (**Fig. 6c**), the H_2O density near the kerogen surface (Zone 2, **Fig. 7c**) is suppressed when salinity is less than 2.03 M. It suggests that the presence of CO_2 has a great influence on the wetting behavior of the kerogen surface. Without CO_2, the kerogen surface exhibits a partially water-wetting feature. With CO_2, kerogen is transformed into a less-water-wetting substrate. However, such a transition is not observed with CH_4. This finding agrees with the previous simulation results [68]. Moreover, as salinity increases, the density of the CO_2 layer decreases. Density profiles in Zone 3 as depicted in **Fig. 7b**, present that CO_2 dissolution within the water/brine cluster is obvious and its solubility is much higher than that of CH_4. Moreover, the ratios of CH_4 and CO_2 uptake in each zone to their total uptake and the corresponding uptake are plotted in **Fig. S2**. As shown in **Fig. S2a**, over 90% of the total CH_4 uptake is contributed by its adsorption in Zone 1, while CO_2 uptake in Zone 2 and Zone 3 contributes more than 20% to the total uptake. As discussed in **Fig. 6a** and **Fig. 7a**, the density distributions in Zone 1 are generally

independent of salinity, while those in Zone 2 and Zone 3 decrease as salinity increases. Therefore, salinity shows a larger effect on the total uptake of CO_2 than that of CH_4.

Following the previous works using completely water-filled nanopores [67,69], we define the CO_2 solubility in confined brine as the sum of gas uptake in Zone 2 and Zone 3. The CO_2 uptake in Zone 2 is included because CO_2 and H_2O can be co-adsorbed in this region (see **Figs. 6** and **7**). The schematic diagram of CO_2 dissolution and the corresponding CO_2 solubility in confined brine under different salinities are given in **Fig. S3**. CO_2 solubility in confined brine is generally three or four times of its bulk solubility, while CO_2 uptake at the kerogen-brine (water) interface (Zone 2) is an important contribution to the over-solubility. A similar phenomenon is also observed in the enhanced CO_2 solubility in hydrophobic kaolinite nanopores under typical geological conditions [67].

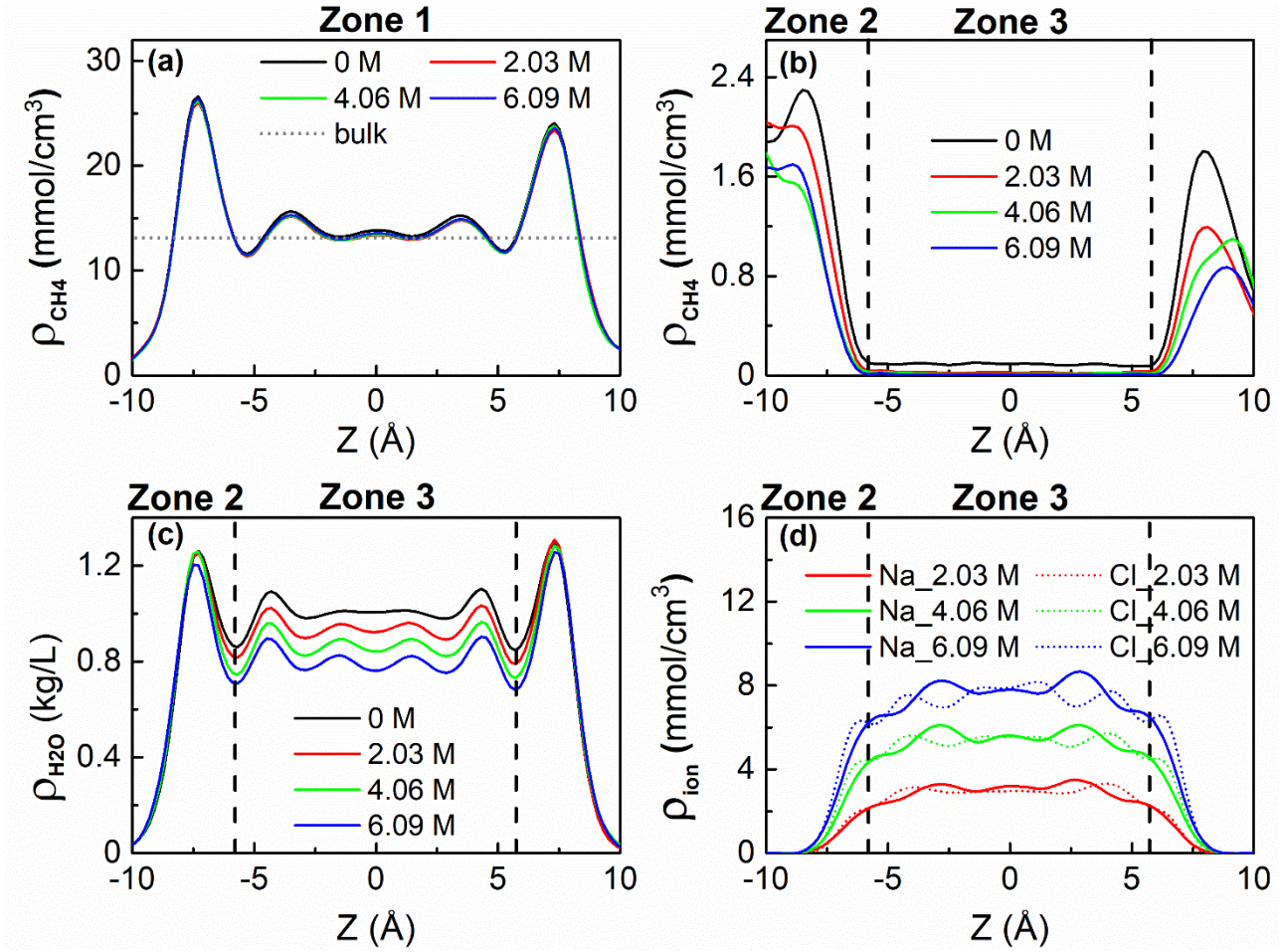

Fig. 6. CH_4 density profiles in (a) Zone 1; (b) Zone 2 and Zone 3; (c) Water; (d) Ion density profiles in Zone 2 and Zone 3 at 338.15 K and 40 MPa. The position Z = 0 Å is the center of the pore.

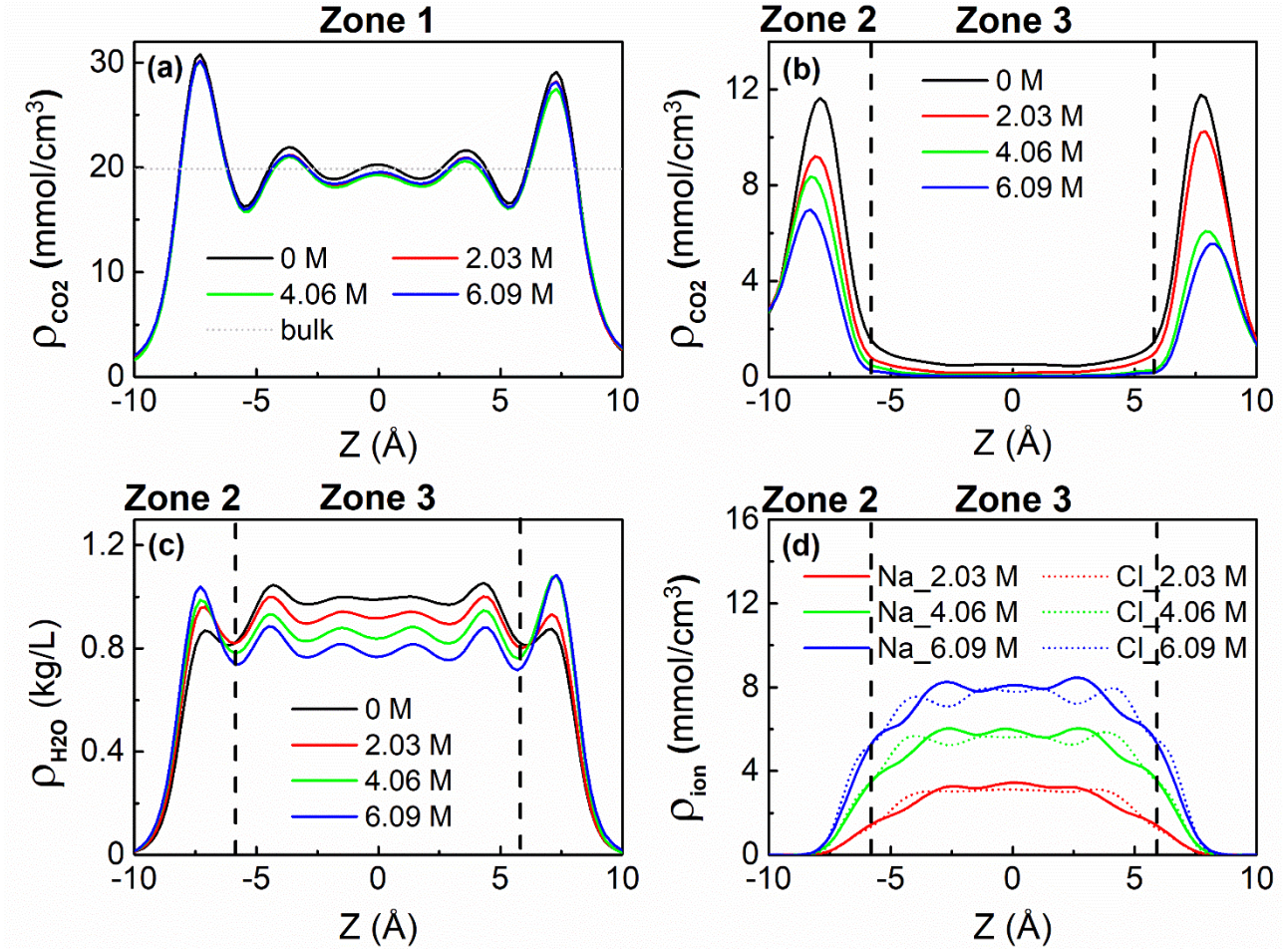

Fig. 7. CO_2 density profiles in (a) Zone 1; (b) Zone 2 and Zone 3; (c) Water; (d) Ion density profiles in Zone 2 and Zone 3 at 338.15 K and 40 MPa. The position Z = 0 Å is the center of the pore.

3.2. Adsorption and dissolution of CH_4/CO_2 mixtures

Gas uptake of CH_4/CO_2 equimolar mixtures in kerogen nanopores filled with brines of varying salinities is also calculated by GCMC simulations. The corresponding snapshots of gas mixtures in the moist kerogen slit pores with different salinities at 338.15 K and 40 MPa are shown in **Fig. S4**. Similar to pure gas adsorption, water/brine clusters form in the kerogen slit pore. We also note that some CO_2 molecules are distributed at the kerogen-brine (water) interface, where CH_4 molecules can hardly be seen. Besides, more CO_2 molecules stay around the brine cluster. **Fig. S5** displays the uptake of CH_4 and CO_2 in the equimolar mixtures as a function of salinity over a wide range of pressures up to 60 MPa. Under the same pressure and temperature condition, a greater uptake of CO_2 over CH_4 is

observed, which can be explained by the stronger fluid-surface affinity. The uptake of CH_4 and CO_2 in the kerogen nanopores almost linearly decreases with salinity.

To explore the effect of salinity on the storage mechanism of CH_4/CO_2 binary mixtures, we present the 2-D density contours of CH_4 and CO_2 at different salinities and 40 MPa in **Fig. 8**. The density distributions of mixtures also conform to the schematic diagram in **Fig. 5i**, which can be divided into three zones. As salinity increases from 0 to 6.09 M, both the CH_4 and CO_2 layers at the kerogen-brine (water) interface (Zone 2) become thinner, although the CH_4 layer is not obvious. In Zone 1, the density distributions of CH_4/CO_2 mixtures are similar to those in pure component adsorption. However, two different phenomena are noticeable for CH_4/CO_2 binary mixtures. As shown in **Fig. 8 (a)** and **(b)**, in the region very close to the brine cluster at X = -22 Å and X = 20 Å (white dashed lines in **Fig. 8**), a thin CO_2 film wraps around the water cluster, where CH_4 density is close to zero. On the other hand, at the CO_2/CH_4/brine (water) interface (the region within the black dotted circles in **Fig. 8b**), a pronounced enhancement in CO_2 density is observed. The same phenomenon is also reflected in **Fig. 8d** at 6.09 M.

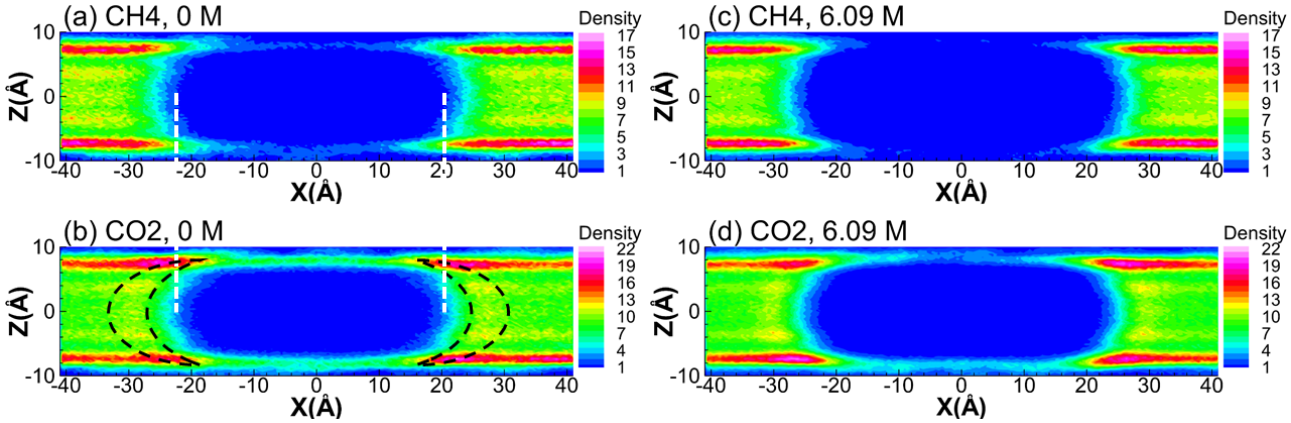

Fig. 8. 2-D Contour plots of CH_4/CO_2 density distributions in 2-nm kerogen slit pores under different salinities: (a) CH_4 and (b) CO_2 at 0 M; (c) CH_4 and (d) CO_2 at 6.09 M at 338.15 K and 40 MPa. The unit of density is mmol/cm^3. The position X = 0 Å, Z = 0 Å dictates the center of the pore.

The density profiles of CH_4 and CO_2 along the *X*-direction are depicted in **Fig. 9a**. In **Fig. 9a**, CO_2 distribution exhibits two peaks at X = ±27.5 Å for a salinity of 0 M, while the CH_4 distribution

presents two shoulders at X = ±29.5 Å. Comparing the positions of the peaks/shoulders in the density profiles of CO_2/CH_4, we observe that CO_2 is closer to the water/brine cluster. This observation is consistent with the 2-D density contours shown in **Fig. 8**. For comparison, density distributions of pure CO_2 and pure CH_4 are also shown in **Fig. 9b** and **Fig. 9c**, respectively. In **Fig. 9b**, the peak in the CO_2 density profiles disappears, suggesting that the CO_2 density is enhanced at the CH_4/CO_2/brine (water) interface, while a slight decrease occurs in the CH_4 density compared to **Fig. 9c**. As salinity increases, the peaks/shoulders of CO_2/CH_4 density distributions migrate towards the directions away from the water/brine cluster and occupy less volume, resulting in a reduced gas uptake. Moreover, the increased salinity also leads to a reduction in the densities of both CO_2 and CH_4 in the center, consisting of the combined densities from Zone 2 and Zone 3.

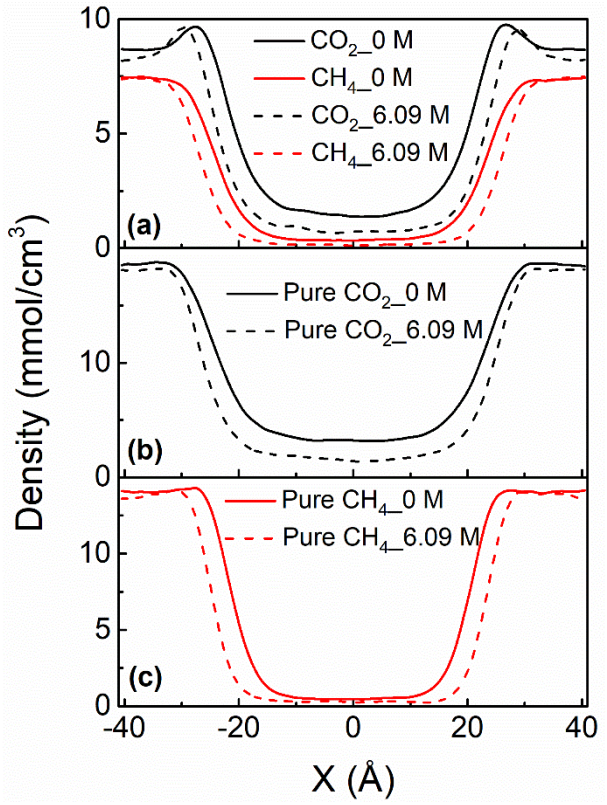

Fig. 9. Density profiles along the *X*-direction of (a) CH_4/CO_2 equimolar mixtures; (b) pure CO_2; (c) pure CH_4 at 338.15 K and 40 MPa.

To clarify the salinity effect on mixture adsorption and dissolution, density profiles of the CH_4/CO_2 binary mixtures in the three zones are illustrated in **Fig. 10**. In **Fig. 10a**, the CO_2 density in

Zone 1 slightly decreases with the addition of NaCl, while the salinity effect on CH_4 density is less pronounced. In terms of the gas dissolution perspective, in Zone 2 (see **Fig. 10b**), both the densities of CH_4 and CO_2 decrease as salinity increases. Besides, salinity has a negative effect on the dissolution of CH_4 and CO_2 in Zone 3. Solubility of CH_4 and CO_2 mixtures in Zone 2 and Zone 3 with increasing salinity is shown in **Fig. S6**. In addition, water density distribution is enhanced near the kerogen surface, when salinity is higher than 0 M (see **Fig. 10b**). With increasing salinity, larger enhancement is observed. This feature is due to the combined effect of CH_4 and CO_2 adsorption.

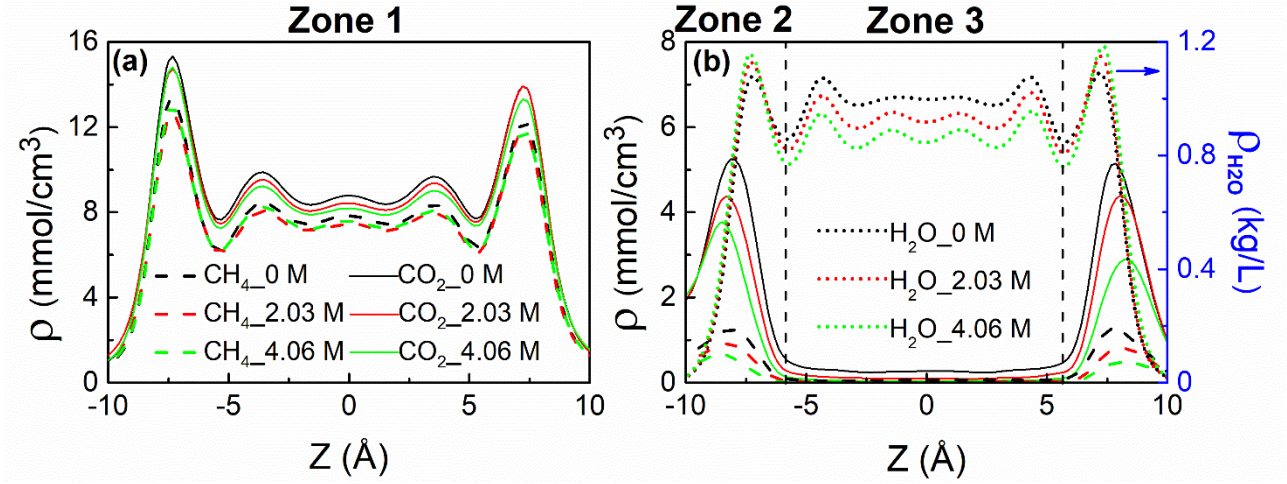

Fig. 10. Density profiles of (a) CH_4/CO_2 binary mixtures in Zone 1; (b) CH_4/CO_2 binary mixtures and water in Zone 2 and Zone 3 at 338.15 K and 40 MPa.

3.3. Implications for shale gas recovery and geological CO_2 sequestration

In the above sections, we investigated the sorption mechanisms of pure gases and their mixtures in moist kerogen nanopores. In this section, we discuss how these results could be applied to improve the efficiency of shale gas recovery and geological CO_2 sequestration. To assess salinity effect on shale gas recovery and geological CO_2 sequestration, a simplified recovery process is proposed as in the previous works [31,70,71]. In this work, the shale gas recovery routine only consists of one traditional pressure drawdown stage and one CO_2 injection stage. **Fig. S7** shows the evolution of CH_4 average density during the shale gas recovery process. A typical shale gas reservoir condition at 338.15 K and an initial pressure of 40 MPa is considered. First, the pressure is dropped from 40 MPa to 20 MPa,

then CO_2 is injected until CO_2 and CH_4 become equimolar in the bulk mixtures. The final pressure is determined by the PR-EOS to be 40.5 MPa.

The CH_4 recovery amount for the two stages and the corresponding CO_2 sequestration amount in different zones under different salinities are presented in **Fig. 11**. With increasing salinity, the CH_4 recovery amount decreases in both pressure drawdown process and CO_2 injection process. Besides, during the pressure drawdown stage, around 89.9% of methane is recovered from the adsorption region as Zone 1, while the ratio is a little higher (93.4%) in the CO_2 injection stage, which suggests that the recovery mainly occurs in Zone 1, especially for CO_2-CH_4 competitive adsorption. This can be explained by the large fraction (~90%) of CH_4 in Zone 1 in the total CH_4 uptake as discussed in **Section 3.1**. Evolution of CH_4 density distributions in the three zones is also depicted in **Figs. S8** and **S9**. In Zone 1 (see **Fig. S8**), CH_4 in the middle of the kerogen slit pores is recovered during the pressure drawdown process, while the injected CO_2 mainly replaces the adsorbed CH_4 from the adsorption layer, which is in line with the previous research [31]. In Zones 2 and 3 (see **Fig. S9**), CH_4 density is relatively low compared to that in Zone 1.

CO_2 sequestration amount also decreases with increasing salinity, as depicted in **Fig. 11b**. As salinity increases, both the uptake of adsorbed gas (Zone 1) and dissolved gas (Zone 2 and Zone 3) decrease. The ratio of each zone to the total CO_2 sequestrated amount is plotted in **Fig. S10**. When salinity is 0 M, around 19.1% of the sequestrated CO_2 is dissolved in Zone 2 and Zone 3. As salinity increases, the ratio of dissolved CO_2 decreases, while that of adsorbed gas slightly increases. The amount of dissolved CO_2 decreases by 14.6%, 24.3% and 33.2% at 2.03 M, 4.06 M and 6.09 M, respectively, which suggests that the presence of brine has a great impact on the solubility trapping of CO_2 sequestration.

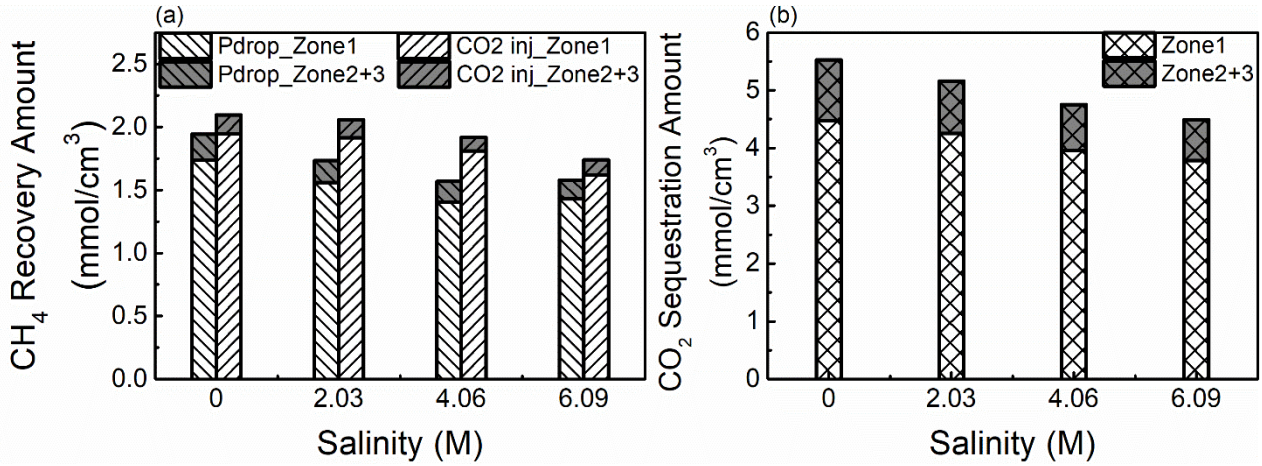

342

343 **Fig. 11.** CH_4 recovery amount (a) and CO_2 sequestration amount (b) in different zones with respect to
344 salinity during the shale gas recovery process in 2-nm kerogen slit pores at 338.15 K.

345 In summary, density distributions of CH_4, CO_2 and their mixtures show that gas uptake in
346 water/brine-filled kerogen nanopores can be divided into three zones, while salinity has a negative
347 effect on the total gas uptake. Gas density distributions in Zone 1 are independent of salinity, but the
348 effective pore volume decreases as salinity increases. In Zone 2 and Zone 3, gas solubility decreases
349 with salinity. CH_4 total uptake is mainly controlled by its adsorption in Zone 1, while CO_2 dissolution
350 in brine (i.e. in Zone 2 and Zone 3) can significantly contribute to its total uptake. For CH_4/CO_2
351 mixtures, CO_2 density is enhanced at the CO_2/CH_4/brine (water) interfaces, while that of CH_4 is slightly
352 reduced due to the stronger affinity of CO_2 to both water and kerogen than CH_4.

353 **4. Conclusions**

354 The ubiquity of brine in shale formations indicates that the study of brine effects in CH_4 and CO_2
355 sorption in kerogen nanopores is essential for the enhanced gas recovery by CO_2 injection and
356 geological CO_2 sequestration in shale reservoirs. In this work, brine effects on the sorption behaviors
357 of pure CH_4, pure CO_2 and their binary mixtures in kerogen slit pores are investigated through GCMC
358 simulations. We find that the gas uptake in water/brine-filled kerogen slit pores can be divided into
359 three distinctive zones and is affected by two mechanisms: adsorption between kerogen surfaces in
360 Zone 1, dissolution at kerogen/water interface as Zone 2 and in water/brines as Zone 3. The total uptake

of CH_4 and CO_2 decreases linearly with increasing salinity. For pure CH_4, CH_4 density in Zone 1 dominates its total uptake. Salinity has little influence on CH_4 density distribution in Zone 1, but results in a decrease in the available pore volume. Salinity effects on CO_2 uptake are profound and delicate. Besides the pore volume decrease in Zone 1, remarkable enhancement in CO_2 solubility in confined brine (in Zone 2 and Zone 3) compared to its bulk solubility is observed, which is mainly contributed by CO_2 uptake in Zone 2. Although the presence of brine occupies the volume for gas adsorption, CO_2 uptake can be compensated to some extent thanks to its high solubility in confined brine. The CO_2 density in Zones 2 and 3 also decreases as salinity increases. Interestingly, with the existence of CO_2 adsorption, the kerogen surface is transformed from a partially water-wetting into a less-water-wetting interface, though this effect is inhibited by the addition of salt. The influence of salinity on the efficiency of shale gas recovery and CO_2 sequestration is also investigated. Increasing salinity leads to decreased amounts of recovered CH_4 and sequestrated CO_2. It is also expected that as brine saturation in kerogen nanopores increases, the contribution of CO_2 dissolution mechanism to the total CO_2 uptake decreases.

Our work provides new insights into the brine effects on CH_4 and CO_2 adsorption in kerogen nanopores partially saturated with brine under shale reservoir conditions in relation to CO_2 enhanced gas recovery and geological CO_2 sequestration. However, in this work, we only considered the pore width of 2 nm, which is a representative of micropores in kerogen, and the condition of partial brine filling. Preliminary studies have shown that pore size plays an important role in gas adsorption kerogen nanopores [27,72]. In addition, the dependence of solubility of CH_4 [32,73] and CO_2 [33,34] in water on pore size has been well documented. In the meantime, kerogen surface wettability is dependent on its maturity [74]. The kerogen surface wettability may have a great influence on the wall/water/gas interaction [75], which can significantly affect gas adsorption and dissolution in kerogen nanopores.

The effects of brine content, pore size and kerogen surface wettability on gas adsorption and dissolution in relation to CO_2 enhanced gas recovery and geological CO_2 sequestrations in shale reservoirs would be explicitly studied in our future work.

5. Acknowledgments

Support from the MOST National Key Research and Development Programme (Project No. 2016YFB0600805) and the Center for Combustion Energy at Tsinghua University is gratefully acknowledged. The simulations were partly performed on the High-Performance Parallel Computer supported by the Tsinghua HPC Platform. Additional support from the UK Engineering and Physical Sciences Research Council under the project UK Consortium on Mesoscale Engineering Sciences (UKCOMES) (Grant No. EP/R029598/1) is gratefully acknowledged. Z. J. acknowledges a Discovery Grant from Natural Sciences and Engineering Research Council of Canada (NSERC RGPIN-2017-05080).

References

[1] S. Walspurger, G.D. Elzinga, J.W. Dijkstra, M. Sarić, W.G. Haije, Sorption enhanced methanation for substitute natural gas production: Experimental results and thermodynamic considerations, Chem. Eng. J. 242 (2014) 379–386. https://doi.org/10.1016/j.cej.2013.12.045.

[2] M. Bui, C.S. Adjiman, A. Bardow, E.J. Anthony, A. Boston, S. Brown, P.S. Fennell, S. Fuss, A. Galindo, L.A. Hackett, J.P. Hallett, H.J. Herzog, G. Jackson, J. Kemper, S. Krevor, G.C. Maitland, M. Matuszewski, I.S. Metcalfe, C. Petit, G. Puxty, J. Reimer, D.M. Reiner, E.S. Rubin, S.A. Scott, N. Shah, B. Smit, J.P.M. Trusler, P. Webley, J. Wilcox, N. Mac Dowell, Carbon capture and storage (CCS): The way forward, Energy Environ. Sci. 11 (2018) 1062–1176. https://doi.org/10.1039/c7ee02342a.

[3] J.S. Loring, E.S. Ilton, C.J. Thompson, P.F. Martin, K.M. Rosso, A.R. Felmy, H.T. Schaef, In Situ Study of CO2 and H2O Partitioning between Na−Montmorillonite and Variably Wet Supercritical Carbon Dioxide, Langmuir. 30 (2014) 6120–6128.

[4] K.C. Schepers, B.C. Nuttall, A.Y. Oudinot, R. Gonazalez, Reservoir Modeling and Simulation of the Devonian Gas Shale of Eastern Kentucky for Enhanced Gas Recovery and CO2 Storage, Soc. Pet. Eng. 126620-MS (2009) 1–20. https://doi.org/10.2118/126620-MS.

[5] K.S. Lackner, A Guide to CO2 Sequestration, Science (80-.). 300 (2003) 1677–1678. https://doi.org/10.1126/science.1079033.

[6] H. Koide, Y. Tazaki, Y. Noguchi, S. Nakayama, M. Iijima, K. Ito, Y. Shindo, Subterranean containment and long-term storage of carbon dioxide in unused aquifers and in depleted natural gas reservoirs, Energy Convers. Manag. 33 (1992) 619–626. https://doi.org/10.1016/0196-8904(92)90064-4.

[7] M. Vandenbroucke, C. Largeau, Kerogen origin, evolution and structure, Org. Geochem. 38

(2007) 719–833. https://doi.org/10.1016/j.orggeochem.2007.01.001.

[8] O.P. Ortiz Cancino, D. Peredo Mancilla, M. Pozo, E. Pérez, D. Bessieres, Effect of Organic Matter and Thermal Maturity on Methane Adsorption Capacity on Shales from the Middle Magdalena Valley Basin in Colombia, Energy and Fuels. 31 (2017) 11698–11709. https://doi.org/10.1021/acs.energyfuels.7b01849.

[9] M. Chen, Y. Kang, T. Zhang, L. You, X. Li, Z. Chen, K. Wu, B. Yang, Methane diffusion in shales with multiple pore sizes at supercritical conditions, Chem. Eng. J. 334 (2018) 1455–1465. https://doi.org/10.1016/j.cej.2017.11.082.

[10] D.M. Jarvie, R.J. Hill, T.E. Ruble, R.M. Pollastro, Unconventional shale-gas systems: The Mississippian Barnett Shale of north-central Texas as one model for thermogenic shale-gas assessment, Am. Assoc. Pet. Geol. Bull. 91 (2007) 475–499. https://doi.org/10.1306/12190606068.

[11] J.B. Curtis, Fractured shale-gas systems, Am. Assoc. Pet. Geol. Bull. 86 (2002) 1921–1938. https://doi.org/10.1306/61EEDDBE-173E-11D7-8645000102C1865D.

[12] P. Charoensuppanimit, S.A. Mohammad, K.A.M. Gasem, Measurements and Modeling of Gas Adsorption on Shales, Energy and Fuels. 30 (2016) 2309–2319. https://doi.org/10.1021/acs.energyfuels.5b02751.

[13] S.M. Kang, E. Fathi, R.J. Ambrose, I.Y. Akkutlu, R.F. Sigal, Carbon Dioxide Storage Capacity of Organic-Rich Shales, SPE J. 16 (2011) 1–14. https://doi.org/10.2118/134583-PA.

[14] R. Heller, M. Zoback, Adsorption of methane and carbon dioxide on gas shale and pure mineral samples, J. Unconv. Oil Gas Resour. 8 (2014) 14–24. https://doi.org/10.1016/j.juogr.2014.06.001.

[15] T.M. Parfenova, A.E. Kontorovich, L.S. Borisova, V.N. Melenevskii, Kerogen from the

443 Cambrian deposits of the Kuonamka Formation (northeastern Siberian Platform), Russ. Geol.
444 Geophys. 51 (2010) 277–285. https://doi.org/10.1016/j.rgg.2010.02.004.
445 [16] G.R. Chalmers, M.R. Bustin, The effects and distribution of moisture in gas shale reservoirs
446 systems, AAPG Annu. Conv. Exhib. (2010) 4.
447 [17] L.F. Ruppert, R. Sakurovs, T.P. Blach, L. He, Y.B. Melnichenko, D.F.R. Mildner, L.
448 Alcantar-Lopez, A USANS/SANS study of the accessibility of pores in the barnett shale to
449 methane and water, Energy and Fuels. 27 (2013) 772–779. https://doi.org/10.1021/ef301859s.
450 [18] D.J.K. Ross, R.M. Bustin, The importance of shale composition and pore structure upon gas
451 storage potential of shale gas reservoirs, Mar. Pet. Geol. 26 (2009) 916–927.
452 https://doi.org/10.1016/j.marpetgeo.2008.06.004.
453 [19] S.M.V. Gilfillan, B.S. Lollar, G. Holland, D. Blagburn, S. Stevens, M. Schoell, M. Cassidy, Z.
454 Ding, Z. Zhou, G. Lacrampe-Couloume, C.J. Ballentine, Solubility trapping in formation
455 water as dominant CO2 sink in natural gas fields, Nature. 458 (2009) 614–618.
456 https://doi.org/10.1038/nature07852.
457 [20] T. Zhang, G.S. Ellis, S.C. Ruppel, K. Milliken, R. Yang, Effect of organic-matter type and
458 thermal maturity on methane adsorption in shale-gas systems, Org. Geochem. 47 (2012) 120–
459 131. https://doi.org/10.1016/j.orggeochem.2012.03.012.
460 [21] G.R.L. Chalmers, R.M. Bustin, The organic matter distribution and methane capacity of the
461 Lower Cretaceous strata of Northeastern British Columbia , Canada, 70 (2007) 223–239.
462 https://doi.org/10.1016/j.coal.2006.05.001.
463 [22] S.M. Kang, E. Fathi, R.J. Ambrose, I.Y. Akkutlu, R.F. Sigal, Carbon dioxide storage capacity
464 of organic-rich shales, SPE J. 16 (2011) 842–855. https://doi.org/10.2118/134583-PA.
465 [23] X. Li, B.M. Krooss, Influence of Grain Size and Moisture Content on the High-Pressure

Methane Sorption Capacity of Kimmeridge Clay, Energy and Fuels. 31 (2017) 11548–11557. https://doi.org/10.1021/acs.energyfuels.7b01298.

[24] M. Gasparik, P. Bertier, Y. Gensterblum, A. Ghanizadeh, B.M. Krooss, R. Littke, Geological controls on the methane storage capacity in organic-rich shales, Int. J. Coal Geol. 123 (2014) 34–51. https://doi.org/10.1016/j.coal.2013.06.010.

[25] M. Gasparik, A. Ghanizadeh, P. Bertier, Y. Gensterblum, S. Bouw, B.M. Krooss, High-pressure methane sorption isotherms of black shales from the Netherlands, Energy and Fuels. 26 (2012) 4995–5004. https://doi.org/10.1021/ef300405g.

[26] A. Busch, S. Alles, Y. Gensterblum, D. Prinz, D.N. Dewhurst, M.D. Raven, H. Stanjek, B.M. Krooss, Carbon dioxide storage potential of shales, Int. J. Greenh. Gas Control. 2 (2008) 297–308. https://doi.org/10.1016/j.ijggc.2008.03.003.

[27] Y. Kurniawan, S.K. Bhatia, V. Rudolph, Simulation of binary mixture adsorption of methane and CO2 at supercritical conditions in carbons, AIChE J. 52 (2006) 957–967. https://doi.org/10.1002/aic.10687.

[28] H. Wu, J. Chen, H. Liu, Molecular dynamics simulations about adsorption and displacement of methane in carbon nanochannels, J. Phys. Chem. C. 119 (2015) 13652–13657. https://doi.org/10.1021/acs.jpcc.5b02436.

[29] T. Zhao, X. Li, Z. Ning, H. Zhao, M. Li, Molecular simulation of methane adsorption on type II kerogen with the impact of water content, J. Pet. Sci. Eng. 161 (2018) 302–310. https://doi.org/10.1016/j.petrol.2017.11.072.

[30] L. Huang, Z. Ning, Q. Wang, W. Zhang, Z. Cheng, X. Wu, H. Qin, Effect of organic type and moisture on CO2/CH4 competitive adsorption in kerogen with implications for CO2 sequestration and enhanced CH4 recovery, Appl. Energy. 210 (2018) 28–43.

https://doi.org/10.1016/j.apenergy.2017.10.122.

[31] J. Zhou, Z. Jin, K.H. Luo, Effects of Moisture Contents on Shale Gas Recovery and CO2 Sequestration, Langmuir. 35 (2019) 8716–8725. https://doi.org/10.1021/acs.langmuir.9b00862.

[32] C.C. Liu, H.J. Chou, C.Y. Lin, D. Janmanchi, P.W. Chung, C.Y. Mou, S.S.F. Yu, S.I. Chan, The oversolubility of methane gas in nano-confined water in nanoporous silica materials, Microporous Mesoporous Mater. 293 (2020) 109793. https://doi.org/10.1016/j.micromeso.2019.109793.

[33] L.N. Ho, Y. Schuurman, D. Farrusseng, B. Coasne, Solubility of Gases in Water Confined in Nanoporous Materials: ZSM-5, MCM-41, and MIL-100, J. Phys. Chem. C. 119 (2015) 21547–21554. https://doi.org/10.1021/acs.jpcc.5b06660.

[34] G. Gadikota, B. Dazas, G. Rother, M.C. Cheshire, I.C. Bourg, Hydrophobic Solvation of Gases (CO2, CH4, H2, Noble Gases) in Clay Interlayer Nanopores, J. Phys. Chem. C. 121 (2017) 26539–26550. https://doi.org/10.1021/acs.jpcc.7b09768.

[35] N.A. Khan, M. Engle, B. Dungan, F.O. Holguin, P. Xu, K.C. Carroll, Volatile-organic molecular characterization of shale-oil produced water from the Permian Basin, Chemosphere. 148 (2016) 126–136. https://doi.org/10.1016/j.chemosphere.2015.12.116.

[36] N. Shrestha, G. Chilkoor, J. Wilder, V. Gadhamshetty, J.J. Stone, Potential water resource impacts of hydraulic fracturing from unconventional oil production in the Bakken shale, Water Res. 108 (2017) 1–24. https://doi.org/10.1016/j.watres.2016.11.006.

[37] B.A. An, Y. Shen, G. Voordouw, Control of sulfide production in high salinity Bakken shale oil reservoirs by halophilic bacteria reducing nitrate to nitrite, Front. Microbiol. 8 (2017). https://doi.org/10.3389/fmicb.2017.01164.

[38] D.E. White, Saline Waters of Sedimentary Rocks, Am. Assoc. Pet. Geol. Mem. 4 (1965) 342–365.

[39] Y. Zhang, D. Shao, J. Yan, X. Jia, Y. Li, P. Yu, T. Zhang, The pore size distribution and its relationship with shale gas capacity in organic-rich mudstone of Wufeng-Longmaxi Formations, Sichuan Basin, China, J. Nat. Gas Geosci. 1 (2016) 213–220. https://doi.org/10.1016/j.jnggs.2016.08.002.

[40] S.C. Löhr, E.T. Baruch, P.A. Hall, M.J. Kennedy, Is organic pore development in gas shales influenced by the primary porosity and structure of thermally immature organic matter?, Org. Geochem. 87 (2015) 119–132. https://doi.org/10.1016/j.orggeochem.2015.07.010.

[41] G.R. Chalmers, R.M. Bustin, I.M. Power, Characterization of gas shale pore systems by porosimetry, pycnometry, surface area, and field emission scanning electron microscopy/transmission electron microscopy image analyses: Examples from the Barnett, Woodford, Haynesville, Marcellus, and Doig uni, Am. Assoc. Pet. Geol. Bull. 96 (2012) 1099–1119. https://doi.org/10.1306/10171111052.

[42] W. Liu, J. Liu, M. Cai, C. Luo, X. Shi, J. Zhang, Pore evolution characteristic of shale in the Longmaxi Formation, Sichuan Basin, Pet. Res. 2 (2017) 291–300. https://doi.org/10.1016/j.ptlrs.2017.03.003.

[43] P. Ungerer, J. Collell, M. Yiannourakou, Molecular modeling of the volumetric and thermodynamic properties of kerogen: Influence of organic type and maturity, Energy and Fuels. 29 (2015) 91–105. https://doi.org/10.1021/ef502154k.

[44] S.R. Kelemen, M. Afeworki, M.L. Gorbaty, M. Sansone, P.J. Kwiatek, C.C. Walters, H. Freund, M. Siskin, Direct Characterization of Kerogen by X-ray and Solid-State 13C Nuclear Magnetic Resonance Methods, Energy and Fuels. 21 (2007) 1548–1561.

https://doi.org/10.1021/ef060321h.

[45] S. Plimpton, Fast Parallel Algorithms for Short-Range Molecular-Dynamics, J. Comput. Phys. 117 (1995) 1–19. https://doi.org/10.1006/jcph.1995.1039.

[46] S.L. Mayo, B.D. Olafson, W.A. Goddard, DREIDING: a generic force field for molecular simulations, J. Phys. Chem. 94 (1990) 8897–8909. https://doi.org/10.1021/j100389a010.

[47] J. Collell, P. Ungerer, G. Galliero, M. Yiannourakou, F. Montel, M. Pujol, Molecular simulation of bulk organic matter in type ii shales in the middle of the oil formation window, Energy and Fuels. 28 (2014) 7457–7466. https://doi.org/10.1021/ef5021632.

[48] K.S. Okiongbo, A.C. Aplin, S.R. Larter, Changes in type II Kerogen density as a function of maturity: Evidence from the Kimmeridge clay formation, Energy and Fuels. 19 (2005) 2495–2499. https://doi.org/10.1021/ef050194+.

[49] M.G. Martin, J.I. Siepmann, Transferable Potentials for Phase Equilibria. 1. United-Atom Description of n-Alkanes, J. Phys.Chem. B. (1998) 2569–2577. https://doi.org/10.1002/aic.15816.

[50] J.J. Potoff, J.I. Siepmann, Vapor-liquid equilibria of mixtures containing alkanes, carbon dioxide, and nitrogen, AIChE J. 47 (2001) 1676–1682. https://doi.org/10.1002/aic.690470719.

[51] H.J.C. Berendsen, J.R. Grigera, T.P. Straatsma, The Missing Term in Effective Pair Potentials, J. Phys. Chem. 91 (1987) 6269–6271. https://doi.org/10.1021/j100308a038.

[52] D.E. Smith, L.X. Dang, Computer simulations of NaCl association in polarizable water, J. Chem. Phys. 100 (1994) 3757–3766. https://doi.org/10.1063/1.466363.

[53] H.A. Lorentz, Ueber die Anwendung des Satzes vom Virial in der kinetischen Theorie der Gase, Ann. Phys. 248 (1881) 127–136. https://doi.org/10.1002/andp.18812480110.

[54] P. Van Der Ploeg, H.J.C. Berendsen, Molecular dynamics simulation of a bilayer membrane,

558 J. Chem. Phys. 76 (1982) 3271–3276. https://doi.org/10.1063/1.443321.
559 [55] I.-C. Yeh, M.L. Berkowitz, Ewald summation for systems with slab geometry, J. Chem. Phys.
560 111 (1999) 3155.
561 [56] B. Coasne, A. Galarneau, F. Di Renzo, R.J.M. Pellenq, Molecular simulation of nitrogen
562 adsorption in nanoporous silica, Langmuir. 26 (2010) 10872–10881.
563 https://doi.org/10.1021/la100757b.
564 [57] B. Widom, Potential-Distribution Theory and the Statistical Mechanics of Flulds, J. Phys.
565 Chem. 715 (1982) 869–872. https://doi.org/10.1021/j100395a005.
566 [58] B. Widom, Some Topics in the Theory of Fluids, 2808 (1963).
567 https://doi.org/10.1063/1.1734110.
568 [59] D. Peng, D.B. Robinson, A New Two-Constant Equation of State, Ind. Eng. Chem. Fundam.
569 15 (1976) 59–64. https://doi.org/10.1021/i160057a011.
570 [60] M.G. Martin, MCCCS Towhee : a tool for Monte Carlo molecular simulation, Mol. Simul. 39
571 (2013) 1212–1222. https://doi.org/10.1080/08927022.2013.828208.
572 [61] O. Talu, A.L. Myers, Molecular simulation of adsorption: Gibbs dividing surface and
573 comparison with experiment, AIChE J. 47 (2001) 1160–1168.
574 https://doi.org/10.1002/aic.690470521.
575 [62] Y. Tian, C. Yan, Z. Jin, Characterization of Methane Excess and Absolute Adsorption in
576 Various Clay Nanopores from Molecular Simulation, Sci. Rep. 7 (2017) 1–21.
577 https://doi.org/10.1038/s41598-017-12123-x.
578 [63] S. Brandani, E. Mangano, L. Sarkisov, Net, excess and absolute adsorption and adsorption of
579 helium, Adsorption. 22 (2016) 1–16. https://doi.org/10.1007/s10450-016-9766-0.
580 [64] H.P. Cady, H.M. Elsey, E. V. Berger, The solubility of helium in water, J. Am. Chem. Soc. 44

581 (1922) 1456–1461. https://doi.org/10.1021/ja01428a009.
582 [65] J. Zhou, Q. Mao, K.H. Luo, Effects of Moisture and Salinity on Methane Adsorption in
583 Kerogen: A Molecular Simulation Study, Energy & Fuels. 33 (2019) 5368–5376.
584 https://doi.org/10.1021/acs.energyfuels.9b00392.
585 [66] X. Zhou, Q. Yuan, Z. Rui, H. Wang, J. Feng, L. Zhang, F. Zeng, Feasibility study of CO 2
586 huff ‘n’ puff process to enhance heavy oil recovery via long core experiments, Appl. Energy.
587 236 (2019) 526–539. https://doi.org/10.1016/j.apenergy.2018.12.007.
588 [67] W. Li, Y. Nan, Z. Zhang, Q. You, Z. Jin, Hydrophilicity/Hydrophobicity Driven CO2
589 Solubility in Kaolinite Nanopores in Relation to Carbon Sequestration, Chem. Eng. J. (2020)
590 125449. https://doi.org/10.1016/j.cej.2020.125449.
591 [68] T.A. Ho, Y. Wang, A. Ilgen, L.J. Criscenti, C.M. Tenney, Supercritical CO2-induced
592 atomistic lubrication for water flow in a rough hydrophilic nanochannel, Nanoscale. 10 (2018)
593 19957–19963. https://doi.org/10.1039/c8nr06204h.
594 [69] L.N. Ho, S. Clauzier, Y. Schuurman, D. Farrusseng, B. Coasne, Gas uptake in solvents
595 confined in mesopores: Adsorption versus enhanced solubility, J. Phys. Chem. Lett. 4 (2013)
596 2274–2278. https://doi.org/10.1021/jz401143x.
597 [70] M. Zhang, S. Zhan, Z. Jin, Recovery mechanisms of hydrocarbon mixtures in organic and
598 inorganic nanopores during pressure drawdown and CO2 injection from molecular
599 perspectives, Chem. Eng. J. 382 (2020) 122808. https://doi.org/10.1016/j.cej.2019.122808.
600 [71] J. Zhou, Z. Jin, K.H. Luo, Insights into recovery of multi-component shale gas by CO2
601 injection: A molecular perspective, Fuel. 267 (2020) 117247.
602 https://doi.org/10.1016/j.fuel.2020.117247.
603 [72] K. Zeng, P. Jiang, Z. Lun, R. Xu, Molecular Simulation of Carbon Dioxide and Methane

Adsorption in Shale Organic Nanopores, Energy and Fuels. 33 (2019) 1785–1796. https://doi.org/10.1021/acs.energyfuels.8b02851.

[73] M. Diaz Campos, Y. Akkutlu, R.F. Sigal, A molecular dynamics study on natural gas solubility enhancement in water confined to small pores, Proc. - SPE Annu. Tech. Conf. Exhib. 4 (2009) 2323–2332. https://doi.org/10.2118/124491-MS.

[74] M. Begum, M.R. Yassin, H. Dehghanpour, Effect of kerogen maturity on organic shale wettability: A Duvernay case study, Mar. Pet. Geol. 110 (2019) 483–496. https://doi.org/10.1016/j.marpetgeo.2019.07.012.

[75] L.O. Lawal, T. Olayiwola, S. Abdel-Azeim, M. Mahmoud, A.O. Onawole, M.S. Kamal, Molecular simulation of kerogen-water interaction: Theoretical insights into maturity, J. Mol. Liq. 299 (2020) 112224. https://doi.org/10.1016/j.molliq.2019.112224.